RSC Applied Polymers

ROYAL SOCIETY OF CHEMISTRY

PAPER

View Article Online
View Journal | View Issue

Check for updates

Cite this: *RSC Appl. Polym.*, 2024, **2**, 1074

Self-limiting electrospray deposition (SLED) of porous polyimide coatings as effective lithium-ion battery separator membranes†

Robert A. Green-Warren,‡[a] Andrew L. Fassler,*‡[b,c] Abigail Juhl,[b] Noah M. McAllister,[a] Andrew Huth,[a] Maxim Arkhipov,[a] Michael J. Grzenda,[a] S. Rahman Pejman,[a] Michael F. Durstock[b] and Jonathan P. Singer *[a]

Electrospray deposition (ESD) is employed to produce separator membranes for coin-cell lithium-ion batteries (LIBs) using off-the-shelf polyimide (PI). The PI coatings are deposited directly onto planar $LiNi_{0.6}Mn_{0.2}Co_{0.2}O_2$ (NMC) electrodes *via* self-limiting electrospray deposition (SLED). Scanning electron microscopy (SEM), optical microscopy, and spectroscopic microreflectometry are implemented in combination to evaluate the porosity, thickness, and morphology of sprayed PI films. Furthermore, ultraviolet-visual wavelength spectroscopy (UV vis) is utilized to qualitatively assess variation in film porosity within a temperature range of 20–400 °C, to determine the stable temperature range of the separator. UV vis results underscore the ability of the SLED PI separator to maintain its porous microstructure up to ~350 °C. Electrochemical performance of the PI separators is analyzed *via* charge/discharge cycle rate tests. Discharge capacities of the SLED PI separators are within 83–99.8% of commercial Celgard 2325 PP/PE/PP separators. This study points to the unique possibility of SLED as a separator manufacturing technique for geometrically complex energy storage systems. Further research is needed to optimize the polymer–solvent system to enhance control of porosity, pore size, and coating thickness. This can lead to significant improvement in rate and cycle life performance in more advanced energy storage devices.

Received 11th June 2024,
Accepted 8th August 2024

DOI: 10.1039/d4lp00192c

rsc.li/rscapplpolym

1. Introduction

Lithium-ion batteries (LIBs) are pervasive in our everyday lives as they are incorporated in everything from electric vehicles to energy storage systems to personal electronics.[1] As such, there is constant motivation to increase the energy density, power density, and lifetime of lithium-ion batteries to power our world. Two key aspects of these types of cells, as well as any improvements to them, are their safety and reliability, which depends on the effectiveness of the separator membrane that physically isolates the positive and negative electrodes of the battery while permitting the electrolyte to transport ions across it.[2] There has been significant research in understanding the failure mechanisms of separators in LIBs, as well as determining the ideal characteristics for safety and performance. Cyclic use of a battery can lead to degradation or failure of this membrane, including blockage of its pores, puncture or shorting from dendritic growth, thermal shrinkage (especially in extreme environments), or mechanical failure.[3–7] In a review paper, Lingappan *et al.* detailed the important characteristics to consider in a LIB separator, including: thickness, porosity and pore size, chemical stability, tortuosity, permeability, wettability and electrolyte uptake, thermal shrinkage, shutdown characteristics, and cost.[2]

To optimize for performance and costs, separator membranes used in LIBs are typically made from blown polyolefin sheets, such as polyethylene (PE) or polypropylene (PP), that are stretched to form a porous structure. This allows for Li-ion transport while simultaneous maintaining separation of the cathode and anode to prevent short circuiting.[8] This manufacturing process is beneficial for mass production of these membranes, but offers limited options in material selection or ability to tune properties, structure, and topography of the

[a]*Department of Mechanical and Aerospace Engineering, School of Engineering, Rutgers University, Piscataway, NJ 08854, USA. E-mail: Jonathan.singer@rutgers.edu*
[b]*Air Force Research Laboratory, Wright-Patterson AFB, OH 45433, USA. E-mail: andrew.fassler.ctr@us.af.mil*
[c]*UES, Inc., Dayton, OH, 45432, USA*

†Electronic supplementary information (ESI) available. See DOI: https://doi.org/10.1039/d4lp00192c

‡R. A. G.-W. and A. L. F. contributed equally to this work.

separator. For this reason, researchers have explored a large variety of techniques to control the characteristics of separator materials and optimize their performance, including phase separation and electrospinning.[9,10] Here, electrospray deposition (ESD) of PI is evaluated as a potential manufacturing approach for separators in planar Li-ion batteries.

ESD consists of applying an electrostatic potential to a liquid solution leading to aerosolization, and ultimately, the production of highly uniform films.[11] Electrosprays occur when an electric potential is applied to a working fluid, where an imbalance of electrostatic charge and surface tension at the surface of the liquid solution results in atomization. Various modes of ESD may occur for sprays with a singular nozzle, such as jetting and multi-jetting – which are standard for delivering continuous ESD films in industrial applications (*e.g.* painting automotive parts). However, many ESD sprays reviewed in literature are generally conducted in the stable Taylor-cone jet mode, since predictable micron and submicron particle sizes may be produced within a narrower size distribution.[12] In this more stable mode, after the initial aerosolization, coulombic explosions cause further breakdown of larger primary droplets into smaller satellite droplets. This phenomenon continues until the droplets reach the spray target where they are deposited directly onto the target substrate. Some core challenges of traditional ESD and other aerosolization techniques, such as ultrasonic spraying, are the lack of control over film and particle morphology, wide particle size distributions, and shadowing effects which can occur with 3D geometrically complex targets.[13,14] These effects can be exacerbated by introducing a parallel flow of air, known as a co-flow, around the spray nozzle to increase coating speeds and surface coverage.[15]

Within ESD, SLED is a unique regime in which amorphous ("glassy") materials are dissolved in highly volatile (*e.g.* low boiling point) solvents to produce porous coatings with tunable microstructures.[13,16,17] In the case of self-limiting electrospray deposition (SLED), incoming droplets are redirected by the repulsive electrostatic forces due to charge accumulated on the surface of the initially deposited film.[13] The final microstructure of the coating ranges from discrete randomly packed particles/fibers to continuous smooth films, and can be selectively tuned by adjusting input spray parameters. Droplet formation is governed largely by the solution properties (*e.g.*, conductivity, viscosity) and ESD parameters (*e.g.*, flow rate, voltage, spray distance).[18] Glassy polymer–solvent blends, addition of inorganic constituents, and the input spray parameters can be selectively manipulated to produce coatings with tailored mechanical properties, film porosity, and functionality.[11,19,20] When evaluating established methods on separator fabrication, SLED is most comparable to electrospinning, another regime within ESD where solid loading of the polymer can be in the range of 5–60 wt%; whereas, polymer concentration for SLED is commonly 1–5 wt%.[16,21] SLED offers many of the advantages of electrospinning, such as compositing and manipulation of feature sizes, but maintains superior control of pore volume, size, and geometry.[22,23] Additionally, SLED enables precise control of layer thickness and conformality, allowing for uniform coatings over both conductive and non-conductive 2D and 3D spray targets.[19,22,24,25]

The glassy polymer highlighted in this research is polyimide (PI) (Matrimid 5218, Huntsman), chosen for its thermal stability, mechanical strength, wettability, and electrochemical performance (see Fig. S3† for molecular structure).[26,27] Carbonyl moieties present in its molecular chain contribute to its hydrophilic behavior, which lends itself well to the adsorption of liquid electrolytes used in LIBs.[28] Additionally, the dielectric properties of Matrimid 5218 provide an amicable electrostatic charge relaxation at the SLED film surface, which enables its thickness limiting behavior (see Fig. S4 in ESI† for a plot displaying self-limiting behavior of PI).[29]

Given its high temperature resistance and mechanical performance, ESD of PI was conducted by Kingsley *et al.* for the production of dielectric barrier coatings for microelectronic devices.[29] Moreover, electrospinning of PI nanowires has been employed to fabricate battery separator membranes with a notable cycle rate of 80 mA h g^{-1} at 5C.[30,31] However, a stepwise temperature ramp up to 300 °C in a vacuum is required for imidization of the electrospun fibers of precursor material to synthesize both neat and composite PI membranes. Additionally, porosity of the electrospun PI separators was measured to be ~90%, more than twice the ideal 40% porosity for commercially available polyolefin separators.[31,32] Electrospun PP mats have been studied and shown to exhibit superior cycle rate performance compared to commercial Celgard 2400; nonetheless, porosity of these separators were limited to ~71%.[33]

Ultimately, electrosprayed PI particles, primarily resembling bead-on-string morphologies, were deposited onto as-purchased $LiNi_{0.6}Mn_{0.2}Co_{0.2}O_2$ (NMC) cathodes in the SLED regime to form a porous coating. Analogs of PI films were deposited onto bare Si wafers for characterization, where microstructure of each film was probed for porosity, particle size, and thickness using microscopy and spectroscopic microreflectometry. Spray coated cathodes were assembled into coin-cells with either lithium metal to form a half-cell or a traditional graphite anode to form a full-cell. Control cells were fabricated using Celgard 2325, a typical separator membrane composed of a tri-layer structure of PP/PE/PP, in place of SLED PI membranes. All cells then underwent various charge and discharge cycles, with C-rates ranging from C/20 to 1C to examine and compare electrochemical performance.

2. Results and discussion

2.1. SLED PI separator characterization

SLED is utilized as the fabrication method for sprayed PI separators in this study as shown in Fig. 1. Requirements for controlled porosity in energy storage applications renders SLED as a viable method for producing porous polymer films with tunable microstructure and functionality for LIBs.[32] Additionally, SLED allows fine tuning of particle morphology, thus enabling control of the mechanical properties, wetting

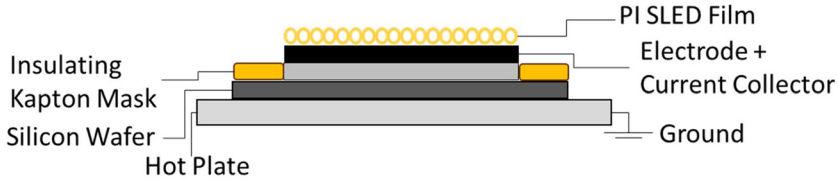

Fig. 1 Illustration of the SLED film deposited onto an electrode. The use of a Kapton tape film mask improves coating uniformity and coverage by redirecting the electrostatic field lines of the spray onto the electrode.

behavior, and ionic transport for separator applications.[16] The spray deposited PI film thickness and porosity is determined *via* a combination of optical microscopy, spectroscopic microreflectometry, and scanning electron microscopy, according to a method developed by McAllister and coworkers for obtaining thickness measurements for highly scattering films.[34]

The SEM images in Fig. 2(a–c) show a cross-sectional view of the PI coated NMC electrode after submersion in N_2 for 10 s and fracturing. The SLED coated electrode is folded in half with the cathodic material externally facing. Fig. 2a highlights a coated electrode, with an aluminum current collector being sandwiched in the middle of the folded electrode. The thickness of the NMC electrode is ~100 μm, while the thickness of the PI film, captured in Fig. 2(b and c), is ~10 μm. This separator thickness is slightly less than that of commercial membranes.[2] Mean porosity was measured by observing the thickness of the film before and after solvent vapor annealing, and found to be ~70%, larger than the typically recommended porosity of 40%.[2] Additionally, the pore size, as seen in Fig. 2c, is on the order of ~1 μm, while the recommended pore size is <1 μm, with many commercial membranes having an average pore size of 30–200 nm. It should be noted that no optimization of the porosity was attempted, so more optimal pore sizes are achievable.[2]

The morphology of the PI particles in Fig. 2(b and c) resemble the bead-on-string morphology previously observed by Lei *et al.*[35] The hydrophilic nature of Matrimid 5218, while an ideal feature for electrolyte uptake, likely contributes to adsorption of ambient moisture.[16,26,36] This can lead to increased viscosity of biphasic PI-solvent droplets, and ultimately, to the morphology of the coating shown in Fig. 2c, as solvent diffusion within the atomized droplet and evaporation become inhibited. It is suspected that this nanowire-like architecture aids in wettability of the liquid electrolyte and is to be explored in greater detail in the future. Notably, Fig. 2b and c demonstrate that the PI film exhibits moderate adhesion to the surface of the NMC. Future work should further explore the effects of co-solvent blends, polymer blends, and environmental controls on the morphology and mechanics of polyimide films produced within this electrospray regime.

To observe changes in porosity as a function of increasing temperature, ultraviolet-visual wavelength spectroscopy (UV vis) was used to measure the diffuse reflectance of the sprayed coating between 20–400 °C, shown in Fig. 3. The prescribed range reflects temperatures commonly seen in LIBs during regular operation through to extreme temperatures that can cause or be caused by thermal runaway.[37] Degradation of the separator membrane can result in contact between the anode and cathode, shorting the circuit and causing catastrophic failure of the battery.

As shown in Fig. 3, inherent variation in film thickness is observed and illustrated by a fluctuation in diffuse reflectance at room temperature (RT), at various positions on the sample, with a characteristic example shown (full data available in the ESI†). While there is some variation in magnitudes of the curve features up until 400 °C, the overall shape of each curve is consistent, indicating that some porosity remains present and the characteristic lengthscale of the pores is maintained. The apparent increase of diffuse reflectance at 350 °C may indicate some reconfiguration of the subwavelength mor-

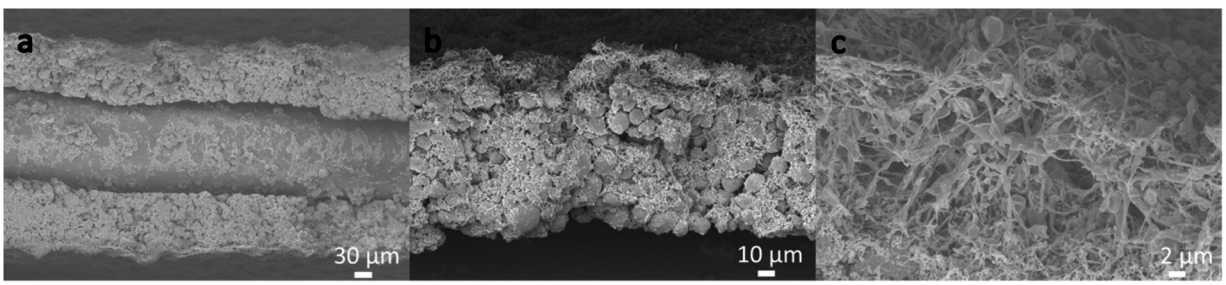

Fig. 2 Cross-sectional SEM images showing (a) top and bottom of fractured PI coated NMC electrode. The middle layer is Al current collector, onto which the cathodic material was deposited. (b) PI coated NMC electrode with PI layer present on the top surface. (c) PI coating morphology displaying a network of particles with characteristic bead-on-string architectures.

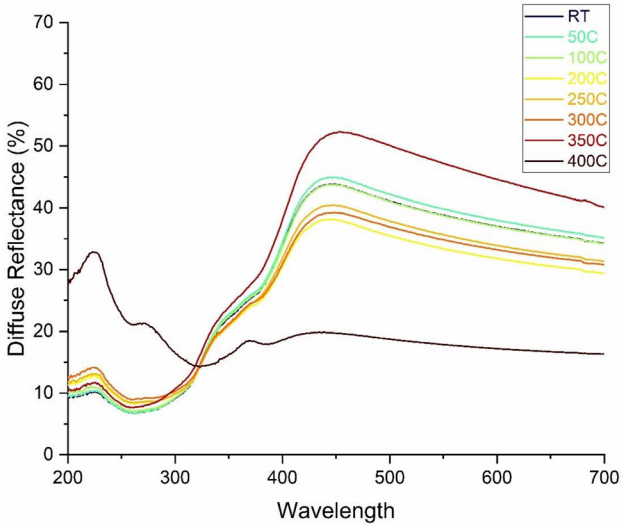

Fig. 3 Diffuse reflectance UV-Vis spectra of SLED PI films on a Si substrate, illustrating the impact of temperature on film porosity. The PI was initially sprayed at RT, then thermally treated for ~10 minutes at each temperature increment, followed by RT UV-Vis spectral analysis for each temperature.

phology. At the 400 °C measurement, a significant decrease in diffuse reflectance is observed at higher wavelengths attributable to thermal decomposition of the polymer and collapse of the pore structure.[32] Concurrently, a significant increase in low wavelength scattering suggests coupled formation of new morphology (*e.g.*, dewetted pinholes) and change of UV index of refraction. This degradation of PI around 400 °C was coupled with smoke generation from the sample after ~5 s on a hotplate. Zhu *et al.* performed a combination of UV vis and DSC, along with various other characterization methods, to evaluate the mechanical properties and thermal stability of smooth PI films.[38] The PI films were synthesized from the pyridine diamine and five aromatic dianhydride monomers *via* a two-step polymerization technique. DSC results from that study, which were limited to a maximum temperature of 350 °C, revealed a T_g of ~300 °C for neat PI films; however, TGA results highlighted a thermal stability up to approximately 450 °C, near which PI begins to thermally decompose.[38] Thus, these results point to the thermal stability of the SLED PI coating at least approaching 350 °C, yielding a greater resistance to thermal meltdown, and improved safety in LIBs containing liquid electrolytes.

2.2. Cycle rate and life cycle

To investigate if the SLED PI material itself had an impact on the electrochemical performance, we first examined half-cells with NMC and lithium metal.[39] Cells were assembled using either a SLED PI coated NMC cathode, or a standard NMC cathode and a Celgard 2325 PP/PE/PP separator. These experiments also included an extra PP/PE/PP separator for both the SLED and control samples so that any changes seen in performance can be attributed to the SLED PI material without concern for shorting.[40] Cells were then cycled from 3 to 4.3 V at different C-rates, beginning with C/20 and increasing every 5 cycles to 1C, as labelled in Fig. 4b. An additional 10 cycles at C/3 are also provided to show recovery from the 1C loading. Looking at the specific capacity, the SLED PI samples performed remarkably similar to that of the control at all cycling rates. Both sets have a capacity loss of ~12% in the initial charge and discharge cycle stemming from side-reactions that occur during formation. After this first cycle, the average C/20 discharge capacity for the SLED PI was only 2.6% less than that of the PP/PE/PP controls at 169.5 mA g^{-1} compared to 174.0 mA g^{-1}. Interestingly, the smallest difference was seen at the 1C rate, where the average discharge capacity is only 0.2% lower, while the biggest divergence was found at C/2, with it being 2.9% less. The voltage curves for the SLED PI (Fig. 4c) and the PP/PE/PP control (Fig. 4c) also appear alike, with only minor additional polarization seen in the SLED PI sample. This may be caused by the difference in pore structure or wetting behavior, and the increase in polarization it may have on the system.

To demonstrate the ability of the SLED PI to act as a standalone separator, it was next implemented into NMC and graphite full-cells. A PP/PE/PP ring was required to cover from the outer edge of the cathode to the inner wall of the coin case to prevent shorting beyond the area of the PI separator (Fig. 5a). Unlike in the half-cells, this added ring does not function as a separator as it does not cover the center where the electrodes overlap. Full-cells were cycled from 2.75–4.2 V following the same C-rate pattern used with the half-cells. We found that functional cells with stable and repeated capacities were achieved using SLED PI as the only separator layer, as shown in Fig. 5b. When compared to the control samples using a PP/PE/PP separator, a noticeable difference between the samples is evident as the C-rate increased. The initial performance, including both the first cycle with its initial loss, as well as the rest of the C/20 cycles, is comparable. The average first cycle loss is 15.1% for the SLED PI samples compared to 16.7% for the controls. These values are larger than that of the half-cells due to the solid electrolyte interphase (SEI) formation that occurs on the graphite anode. In the following C/20 cycles, the SLED PI cells show an average discharge capacity of 158.3 mA g^{-1}, 2.0% less than that of the PP/PE/PP controls (161.5 mA g^{-1}). This worsened with each rate increase to a maximum difference of 17% at 1C. Importantly, the voltage curves for the SLED PI (Fig. 5c) do show the expected profiles for graphite and NMC cells. However, the reduced performance is apparent when compared to the PP/PE/PP control (Fig. 5d), as is increased polarization.

Regardless of this reduced performance, this remains a significant achievement as the first SLED separator. This deposition technique offers a significant advantage over other electrospray techniques in that it is self-limiting, thus more uniform layers can be achieved. Furthermore, the system presented used the materials as received, leaving significant space for improvement and specialization toward future target appli-

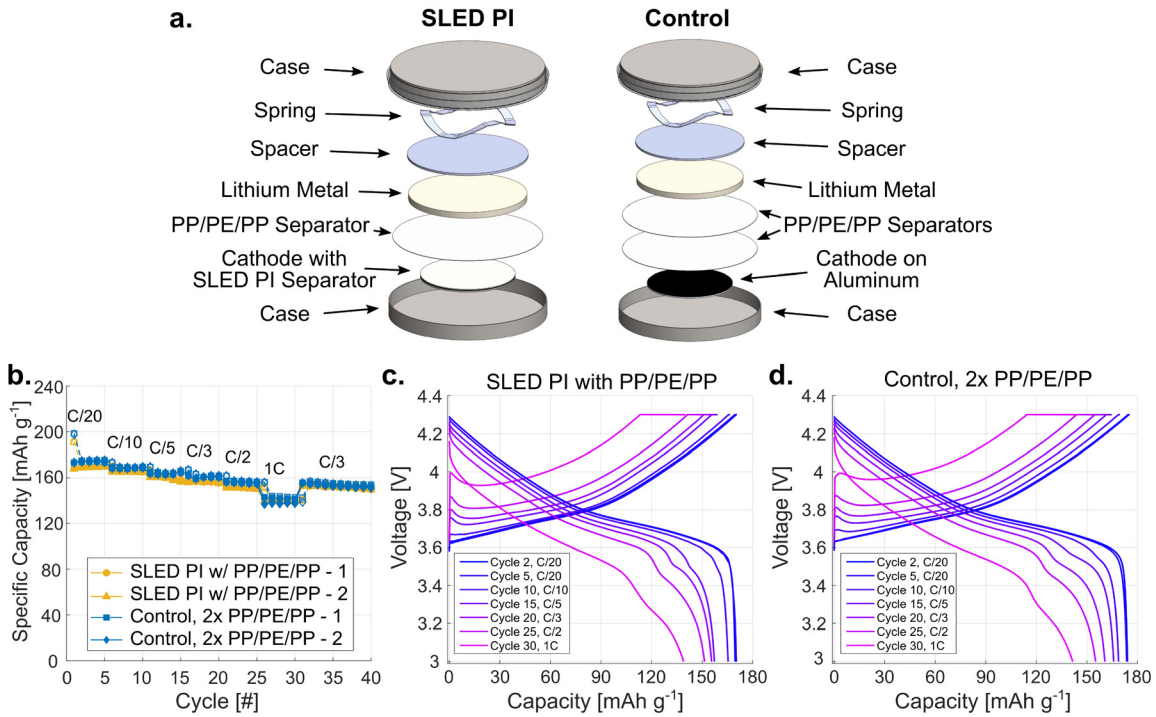

Fig. 4 Cycling performance of SLED PI and control half-cells. (a) Schematic of half-cell assemblies for SLED PI and control cells. (b) Specific capacity as a function of cycle number and C-rate. Hollow markers indicate charge capacity and filled markers indicate discharge capacity. Voltage profiles for the different C-rates for (c) a SLED PI half-cell and (d) a control sample with only PP/PE/PP separators.

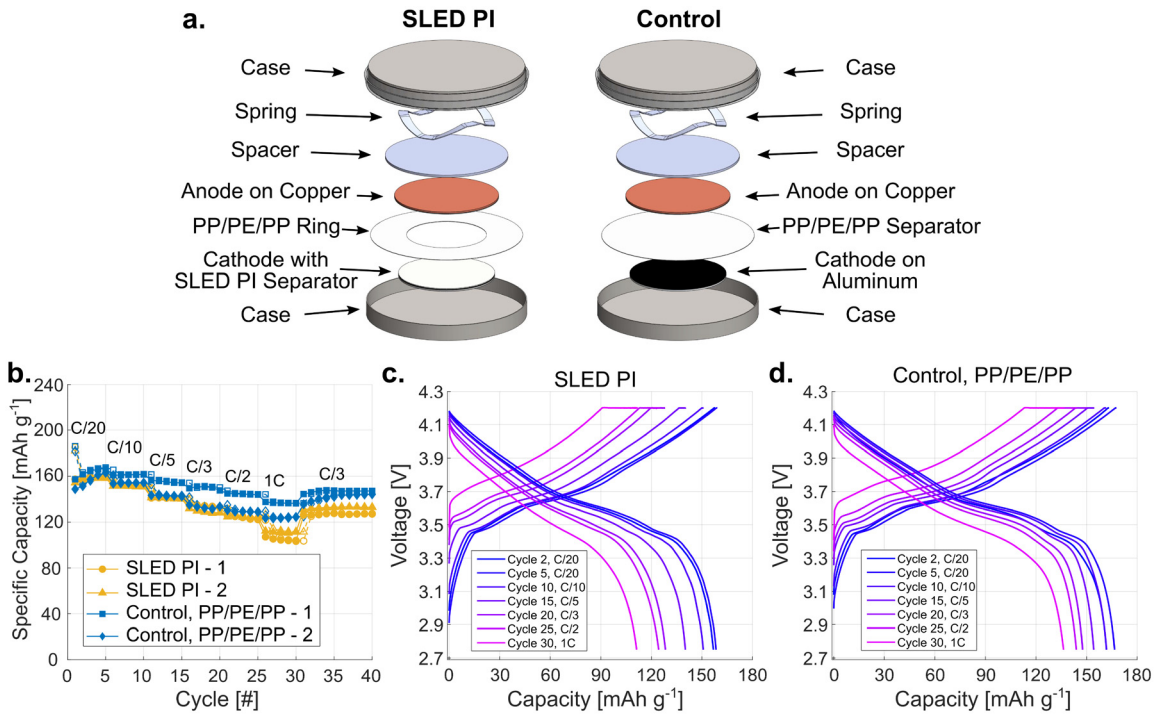

Fig. 5 Cycling performance of SLED PI and control full-cells. (a) Schematic of full-cell assemblies for SLED PI and control cells. (b) Specific capacity as a function of cycle number and C-rate. Hollow markers indicate charge capacity and filled markers indicate discharge capacity. Voltage profiles for the different C-rates for (c) a SLED PI full-cell and (d) a control sample with only a PP/PE/PP separator.

cations. Two such applications of interest include: continuous separator coatings in roll-to-roll manufacturing to simplify assembly for large scale cell production; and coverage of complex geometry and 3D printed cells to provide a conformal and integrated separator layer.

Future work should examine controlling the morphology of SLED materials, how this impacts the porous network, and if it can be tuned to improve ion transport and reduce polarization. A significant part of this will include adapting the materials and process specifically for this separator application. For example, variance in PI particle morphology is expected to have significant correlation to the overall performance of the SLED coated cells. The polymer–solvent system implemented (PI in dichloroethane (DCE) and chloroform) can exhibit hydrophilic behavior due to terminated hydroxyl groups in the polyimide chain.[26] These hydroxyl groups tend to absorb ambient humidity which may contain ionized water due to particulates. By increasing solution viscosity and inhibiting solvent evaporation, this can adversely affect both in-air atomization and charge dissipation upon deposition of the droplets onto the grounded target. This can be overcome by utilizing hydrophobic co-solvents and/or co-polymer blends, or fabricating the SLED coatings in a controlled environment, as is typically done for ESD of bioactive materials.[17] By incorporating changes such as this, we hope to build on the successful demonstration shown here and maximize the performance of future iterations.

3. Conclusion

This work demonstrates the efficacy of employing ESD in the SLED regime to deposit porous PI coatings as separator membranes in LIBs using commercially available materials. The utility of ESD applied to LIBs is affirmed by the cyclic charge/discharge performance of the SLED separator. The SLED PI material performed very similarly to the commercial Celgard 2325 separator in half-cells at all rates, its worst discharge capacity being 97.1% of the PP/PE/PP samples at the C/2 rate. In full-cells, the SLED PI's performance was best at slow rates, where its discharge capacity was 98% that of the PP/PE/PP samples at C/20. At our maximum rate of 1C, discharge capacity was 83% of the samples with the commercial separator. Further, UV-vis experiments performed on SLED PI films on Si wafers that had been thermally annealed between 20–400 °C highlight the thermal stability and integrity of PI, with no significant changes in diffuse reflectance until ~350 °C. Mean porosity, pore size, and film thickness were found to be ~70%, on the order of ~1 μm, and ~20 μm, respectively, using a combination of optical microscopy, SEM, and spectroscopic microreflectometry. Notably, the pore parameters deviate from the recommended values of 40% and less than 1 μm for porosity and pore size, as commonly found in commercial separators, and are likely a cause of underperformance when compared to the control PP/PE/PP samples.[2] However, it is also important to recognize that the Matrimid 5218 PI was not modified for the SLED process or its application as a battery separator.

Future research should seek to optimize the properties of the polymer–solvent system, such as boiling point, solution conductivity, and dielectric properties for SLED. Maintaining finer control over pore size, porosity, and morphology of SLED separators would likely improve charge/discharge capacity and cycle life performance, two key metrics for LIBs. Further, probing of the mechanical properties of SLED separators at elevated temperatures up to 400 °C would inform energy storage researchers on how to minimize mechanical failure of ESD separators used in LIBs. SLED is well positioned as a facile technique for the generation of PI battery separators and poses as a promising alternative to electrospinning, phase separation, and blowing techniques currently used due to precise control of thickness, morphology, and porosity. With further refinement, SLED may be a suitable method for depositing conformal separators onto more complex 2D and 3D energy storage architectures produced *via* additive manufacturing.

4. Experimental methods

4.1. Materials

All materials were used as received. The polyimide (Matrimid 5218) used in this study was acquired from Huntsman Corporation (Texas, USA) and selected for its solubility in chlorinated solvents. Dichloroethane (DCE) and chloroform were obtained from Sigma Aldrich. Solutions of 0.2% PI in DCE and 0.2% PI in chloroform were blended in a 2 : 1 v/v ratio. The 0.2% PI in 2 : 1 DCE : chloroform solution was the choice solvent system based on PI solubility, volatility, and ability to produce a stable Taylor cone jet spray while in the SLED regime. High voltage AC–DC power supply systems (0–30 kV) were procured from Acopian Technical Co. (Pennsylvania, USA).

Electrode materials were purchased from NEI Corporation. The NANOMYTE® BE-200E natural graphite anode material has an areal loading of 8.77 mg cm^{-2} (90% active material, 5% PVDF binder, 5% Super P) on 10 μm thick copper foil. The NANOMYTE® BE-54E $LiNi_{0.6}Mn_{0.2}Co_{0.2}O_2$ (NMC) cathode material has an areal loading of 16.47 mg cm^{-2} (90% active material, 5% PVDF binder, 5% Super P) on 16 μm thick aluminum foil. Lithium metal discs with a diameter of 15.6 mm and 0.45 mm thickness were purchased from MTI Corporation. The 2025 coin cell cases were purchased from AME Energy Co. LP40 electrolyte (1 M $LiPF_6$ in ethylene carbonate : diethyl carbonate 1 : 1 by weight) was purchased from Gotion.

4.2. Electrospray system

The electrospray system utilized in this study is identical to that used in previous studies on SLED in ambient environments.[13,16,17,20,34] Please see references for details.

4.3. Electrospray process parameters

A 0.2 wt% solution of Matrimid 5218 was dissolved in 2 : 1 volumetric ratio of dichloroethane (DCE) to chloroform. Each sample was sprayed at 0.2 mL h^{-1} for ~12 hours, resulting in a total mass of ~4.8 mg of PI per sample. The electrode was mounted to a boron doped p-type silicon wafer (University Wafer, USA) using a small strip of pre-pressured double-sided carbon tape. The carbon tap was pressed by hand to limit adhesion to the current collector and electrode; this was done to mitigate damage of the electrode upon removal from the Si wafer. The nozzle and extractor distances were set to 4 and 5 cm, respectively. The voltage applied to the nozzle and extractor ring, respectively, was ~5.0 and ~0.2 kV with a positive polarity. Fabrication was done in a fume hood under ambient conditions with an average temperature of ~22 °C and a relative humidity between 23–34%.

4.4. SLED separator characterization

Analog PI films, sprayed at identical parameters to that of the electrodes, were deposited onto bare Si wafers for characterization. Thickness measurements of the porous SLED films were taken using cross-sectional optical microscopy. Subsequent solvent vapor annealing was completed for five minutes over a chloroform bath. Finally, a Filmetrics F40 spectroscopic microreflectometer (Filmetrics Inc., USA) was utilized to measure thickness of the densified PI film. Porosity was then calculated from the porous and dense thickness values, assuming constant material mass and volume upon annealing.

Post-spray, PI coated NMC electrodes were submerged in N_2 for 10 s and fractured to prepare for SEM. The spray coated electrode is folded in half with the anodic material facing outwardly. The coated electrodes were mounted on flat SEM pucks using double sided carbon tape and coated with 10 nm of Au *via* gold sputtering. SEM was then conducted on a Zeiss FESEM Gemini 300 (Zeiss, Germany) with a 5 kV accelerating voltage. The working distance was set to ~14 mm to optimize for both resolution and depth-of-field.

Lastly, ultraviolet-visual wavelength spectroscopy (UV vis) (Jasco V770) was used to qualitatively observe the evolution of porosity of the PI film with increasing temperature. A single PI sample was sprayed at ambient conditions, thermally soaked for ~10 min, and finally measured at several locations *via* UV-Vis. Multiple measurements were taken at RT to minimize error due to variations in surface roughness. These procedures were repeated for the following temperature steps: RT, 50, 100, 200, 250, 300, 350, and 400 °C.

4.5. Electrode preparation

Electrode materials were punched to size using a 13 mm metal punch for the graphite anode and a 12 mm metal punch for the NMC cathode. NMC cathodes with a SLED coating were punched after deposition of the PI. Celgard 2325 PP/PE/PP separators were punched using a 19 mm metal punch. PP/PE/PP rings, used to prevent shorting between the spacer and coin case when a full separator is not used, were prepared by cutting a 10 mm diameter hole into a 19 mm separator using a pen knife and stencil. All materials were dried overnight (>16 hours) in a vacuum oven at 60–80 °C and under house vacuum (−25 inHg gauge pressure), and then transferred to the glovebox.

4.6. Cell assembly

Assembly of cells was performed in an argon atmosphere with <1 ppm of O_2 and H_2O. Half-cell control samples were fabricated using a lithium metal disc, an NMC cathode, and two PP/PE/PP separators. Half-cell experimental samples were fabricated using a lithium metal disc, a SLED PI coated NMC cathode, and a single PP/PE/PP separator. Full-cell control samples were fabricated using a graphite anode, an NMC cathode, and single PP/PE/PP separator. Full-cell experimental samples were fabricated using a graphite anode, a SLED PI coated NMC cathode, and a PP/PE/PP ring. The ring is necessary to prevent shorting between the spacer and case as the SLED PI coating only prevents shorting between the electrodes. LP40 electrolyte was used in all samples. Coin cells were sealed using a Gelon Electric Coin Cell Crimper Machine (GN-CC20E). After assembly, all cells are allowed to rest at 30–32 °C for at least 24 hours to allow for the electrolyte to fully wet the electrodes.

4.7. Electrochemical characterization

Cycling of cells was performed using either a Series 4000 or Series 4200 Maccor Automated Test System at room temperature. Half-cells were cycled between 3.0–4.3 V and allowed to rest for 8 hours on the test system before charging. Full-cells were cycled between 2.75–4.2 V. In the initial charge for full-cells, samples were brought to 2.75 V and then allowed to rest for 8 hours before resuming charging. Cells were charged using constant current constant voltage (CCCV) with a 0.05C current limit (0.025 current limit for C/20 rate) and galvanostatically discharged. After each charge or discharge, cells were allowed to rest for 30 minutes. Samples underwent 5 cycles each of C/20, C/10, C/5, C/3, C/2, and 1C followed by cycling at C/3. C-rates for cells were determined using the NMC content of the cell and calculated using a specific capacity of 166 mA h g^{-1}, as observed in preliminary testing. The specific capacity of the graphite was taken to be 340 mA h g^{-1}, resulting in an N/P ratio of 1.08.

Conflicts of interest

There are no conflicts to declare.

Acknowledgements

This work was partially funded by the NSF through CMMI Award 2019849. R. A. G.-W. acknowledges support from the National GEM Consortium and the Department of Defense SMART Scholarship Program. N. M. M. acknowledges support

from the New Jersey Space Grant Consortium, funded by NASA, through the student fellow program. A. L. F. acknowledges support from the Air Force Office of Scientific Research (grant no. 16RXCOR320).

References

1 T. Kim, W. Song, D.-Y. Son, L. K. Ono and Y. Qi, *J. Mater. Chem. A*, 2019, **7**, 2942–2964.
2 N. Lingappan, W. Lee, S. Passerini and M. Pecht, *Renewable Sustainable Energy Rev.*, 2023, **187**, 113726.
3 H. Yoneda, Y. Nishimura, Y. Doi, M. Fukuda and M. Kohno, *Polym. J.*, 2010, **42**, 425–437.
4 Q. Yun, Y.-B. He, W. Lv, Y. Zhao, B. Li, F. Kang and Q.-H. Yang, *Adv. Mater.*, 2016, **28**, 6932–6939.
5 M. Held, M. Tuchschmid, M. Zennegg, R. Figi, C. Schreiner, L. D. Mellert, U. Welte, M. Kompatscher, M. Hermann and L. Nachef, *Renewable Sustainable Energy Rev.*, 2022, **165**, 112474.
6 Q. Wang, P. Ping, X. Zhao, G. Chu, J. Sun and C. Chen, *J. Power Sources*, 2012, **208**, 210–224.
7 B. Liu, Y. Jia, C. Yuan, L. Wang, X. Gao, S. Yin and J. Xu, *Energy Storage Mater.*, 2020, **24**, 85–112.
8 P. Arora and Z. J. Zhang, *Chem. Rev.*, 2004, **104**, 4419–4462.
9 J.-H. Liu, P. Wang, Z. Gao, X. Li, W. Cui, R. Li, S. Ramakrishna, J. Zhang and Y.-Z. Long, *Renewable Sustainable Energy Rev.*, 2024, **189**, 113939.
10 A. J. Manly and W. E. Tenhaeff, *J. Mater. Chem. A*, 2022, **10**, 10557–10568.
11 J. Zeleny, *Phys. Rev.*, 1917, **10**, 1–6.
12 G. I. Taylor, *Proc. R. Soc. London, Ser. A*, 1964, **280**, 383–397.
13 L. Lei, D. A. Kovacevich, M. P. Nitzsche, J. Ryu, K. Al-Marzoki, G. Rodriguez, L. C. Klein, A. Jitianu and J. P. Singer, *ACS Appl. Mater. Interfaces*, 2018, **10**, 11175–11188.
14 L.-H. Chou, X.-F. Wang, I. Osaka, C.-G. Wu and C.-L. Liu, *ACS Appl. Mater. Interfaces*, 2018, **10**, 38042–38050.
15 F. Sultan, E. Allaf-Akbari and N. Ashgriz, *Aerosol Sci. Eng.*, 2020, **4**, 210–218.
16 R. A. Green-Warren, L. Bontoux, N. M. McAllister, D. A. Kovacevich, A. Shaikh, C. Kuznetsova, M. Tenorio, L. Lei, A. A. Pelegri and J. P. Singer, *ACS Appl. Polym. Mater.*, 2022, **4**, 3511–3519.
17 S. H. Park, L. Lei, D. D'Souza, R. Zipkin, E. T. DiMartini, M. Atzampou, E. O. Lallow, J. W. Shan, J. D. Zahn, D. I. Shreiber, H. Lin, J. N. Maslow and J. P. Singer, *Nat. Commun.*, 2023, **14**, 4896.
18 A. M. Gañán-Calvo, J. Dávila and A. Barrero, *J. Aerosol Sci.*, 1997, **28**, 249–275.
19 D. A. Kovacevich, L. Lei, D. Han, C. Kuznetsova, S. E. Kooi, H. Lee and J. P. Singer, *ACS Appl. Mater. Interfaces*, 2020, **12**, 20901–20911.
20 Z. Ren, R. Green-Warren, N. McAllister, A. Kim, A. Shaikh, A. A. Pelegri, J. P. Singer and J.-H. Lee, *Giant*, 2023, **15**, 100180.
21 J. Xue, T. Wu, Y. Dai and Y. Xia, *Chem. Rev.*, 2019, **119**, 5298–5415.
22 J. M. Blisko, M. J. Grzenda, R. M. Vladimirsky, C. E. Shuck, J. P. Singer and X. Yong, *Nanoscale*, 2022, **14**, 17985–17994.
23 S. Huang, J. Mansouri, P. Le-Clech, G. Leslie, C. Y. Tang and A. G. Fane, *J. Membr. Sci.*, 2022, **646**, 120248.
24 M. J. Grzenda, M. Atzampou, A. Samateh, A. Jitianu, J. D. Zahn and J. P. Singer, *Coatings*, 2023, **13**, 599.
25 A. Rouf, S. H. Park and J. P. Singer, *Adv. Mater. Interfaces*, 2024, 2300982.
26 J. Yin, H. Hui, B. Fan, J. Bian, J. Du and H. Yang, *Membranes*, 2022, **12**, 592.
27 M. Zhang, L. Wang, H. Xu, Y. Song and X. He, *Nano-Micro Lett.*, 2023, **15**, 135.
28 T. Wu, J. Dong, F. Gan, Y. Fang, X. Zhao and Q. Zhang, *Appl. Surf. Sci.*, 2018, **440**, 595–605.
29 B. J. Kingsley and P. R. Chiarot, *ACS Appl. Polym. Mater.*, 2023, **5**, 1797–1809.
30 S. Wang, Z. Ma, W. Zhao, W. Zhang, C. Li, S. Yang, J. Liu, Z. Guo, H. Zhao and L. Ren, *ACS Appl. Mater. Interfaces*, 2022, **14**, 47578–47586.
31 Y. Wang, S. Wang, J. Fang, L.-X. Ding and H. Wang, *J. Membr. Sci.*, 2017, **537**, 248–254.
32 J. Jang, J. Oh, H. Jeong, W. Kang and C. Jo, *Materials*, 2020, **13**, 4625.
33 Z. Zou, Y. Wei, Z. Hu and H. Pu, *Chem. Eng. J.*, 2023, **474**, 145724.
34 N. M. McAllister, R. A. Green-Warren, M. Arkhipov, J.-H. Lee, A. A. Pelegri and J. P. Singer, *Eng. Rep.*, 2023, e12830.
35 L. Lei, S. Chen, C. J. Nachtigal, T. F. Moy, X. Yong and J. P. Singer, *Mater. Horiz.*, 2020, **7**, 2643–2650.
36 S. Zhang, W. Li, J. Luan, A. Srivastava, V. Carnevale, M. L. Klein, J. Sun, D. Wang, S. P. Teora, S. J. Rijpkema, J. D. Meeldijk and D. A. Wilson, *Nat. Chem.*, 2023, **15**, 240–247.
37 J. C. Kelly, N. L. Degrood and M. E. Roberts, *Chem. Commun.*, 2015, **51**, 5448–5451.
38 Z. Li, Y. Wang and S. Zhu, *J. Phys.: Conf. Ser.*, 2021, **1732**, 012126.
39 B. Rowden and N. Garcia-Araez, *Energy Rep.*, 2021, **7**, 97–103.
40 V. Murray, D. S. Hall and J. R. Dahn, *J. Electrochem. Soc.*, 2019, **166**, A329.